ELECTRONIC SUPPLEMENTARY INFORMATION

A bifunctional catalyst based on carbon quantum dots/mesoporous $SrTiO_3$ heterostructure for cascade photoelectrochemical nitrogen reduction

Yongming Hu,[a] Zhi Liang Zhao,[b] Rafia Ahmad,[c] Moussab Harb,[c] Luigi Cavallo,[c] Luis Miguel Azofra,[d,*] San Ping Jiang,[e] and Xinyi Zhang[a,b,*]

[a] Hubei Key Laboratory of Ferro- & Piezoelectric Materials and Devices, School of Physics and Electronic Science, Hubei University, Wuhan, 430062, China

[b] Foshan Xianhu Laboratory of the Advanced Energy Science and Technology Guangdong Laboratory, Foshan 528216, China

[c] KAUST Catalysis Center (KCC), King Abdullah University of Science and Technology (KAUST), 4700 KAUST, Thuwal 23955-6900, Saudi Arabia

[d] Instituto de Estudios Ambientales y Recursos Naturales (i-UNAT), Universidad de Las Palmas de Gran Canaria (ULPGC), Campus de Tafira, 35017, Las Palmas de Gran Canaria, Spain

[e] Western Australian School of Mines: Minerals, Energy and Chemical Engineering, Curtin University, Perth, WA 6845, Australia

Corresponding authors: xinyizhang@hubu.edu.cn; luismiguel.azofra@ulpgc.es

Supplemental Figures

Figure S1. Schematic illustration of the fabrication process of CQDs/STO heterostructure.

Figure S2. SEM image of conventional cubic STO nanoparticles, exhibiting a flat nonporous surface.

Figure S3. High angle annular dark field scanning TEM (HAADF-STEM) and high-magnification TEM images of mesoporous STO.

Figure S4. (a) UV-Vis spectra and (b) calibration curve obtained for standard ammonia solutions with a series of standard concentration.

Figure S5. Photocatalytic stability test for six successive cycles on STO and CQDs/STO. The solution was refreshed every 1 hour..

Figure S6. Yield rate of ammonia obtained on (i) STO and (ii) CQDs/STO (in Ar atmosphere under 1 sun illumination) and (iii) STO and (iv) CQDs/STO (in N_2 atmosphere in dark) over 12 h.

Figure S7. Optimized structures of the models used for the DFT analysis. Defective STO and composite STO/CQD structures have been prepared from these ones.

Figure S8. Proposed reaction mechanism for the electrochemical N_2 conversion into NH3 catalyzed by the STO(200) surface with two O-vacancies in parallel. Note: reaction free energies at room temperature are shown in eV when there is no applied potential (U = 0) and pH = 0.

Figure S9. Proposed reaction mechanism for the electrochemical N_2 conversion into NH3 catalyzed by the STO(200) surface with two O-vacancies in line. Note: reaction free energies at room temperature are shown in eV when there is no applied potential (U = 0) and pH = 0.

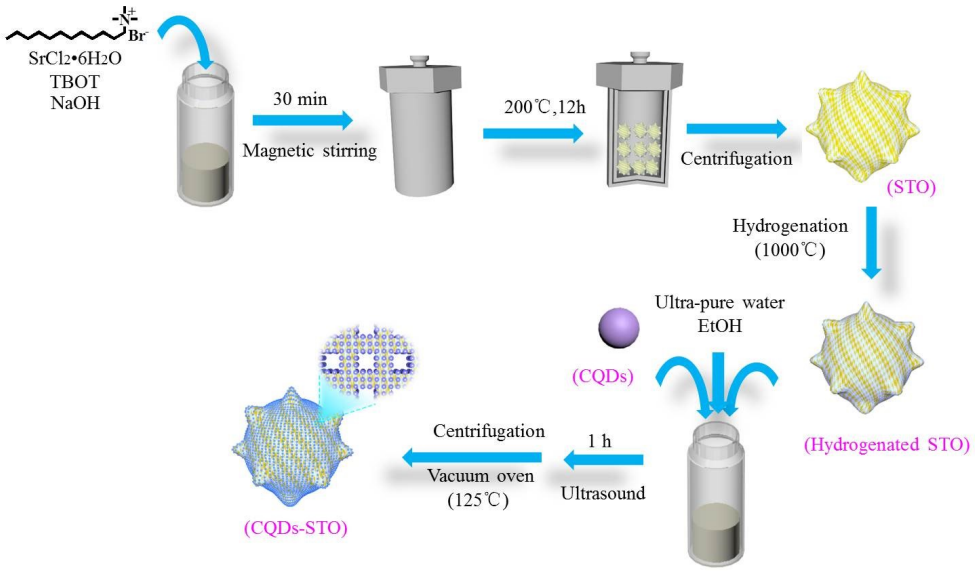

Figure S1. Schematic illustration of the fabrication process of CQDs/STO heterostructure.

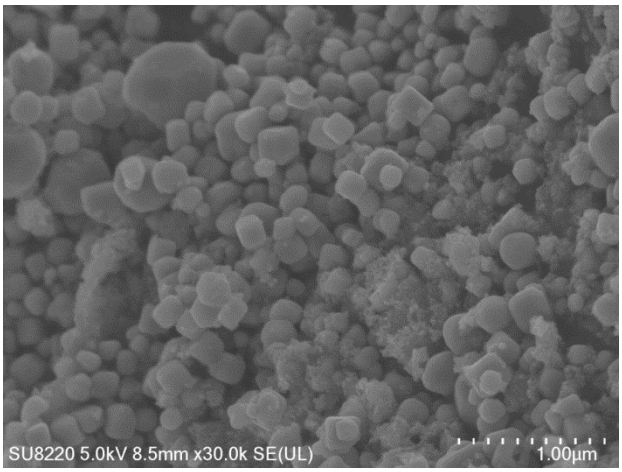

Figure S2. SEM image of conventional cubic STO nanoparticles, exhibiting a flat nonporous surface.

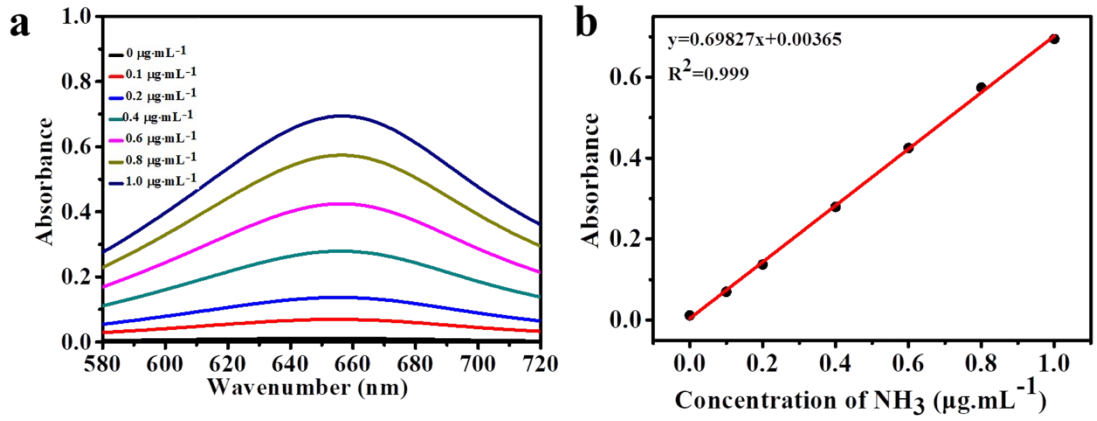

Figure S3. (a) UV-Vis spectra and (b) calibration curve obtained for standard ammonia solutions with a series of standard concentration.

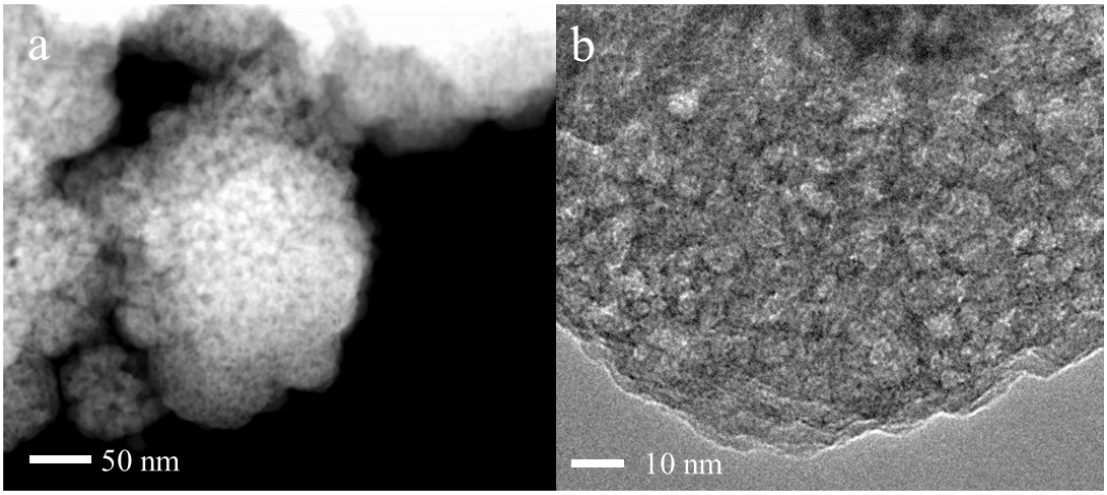

Figure S4. High angle annular dark field scanning TEM (HAADF-STEM) and high-magnification TEM images of mesoporous STO.

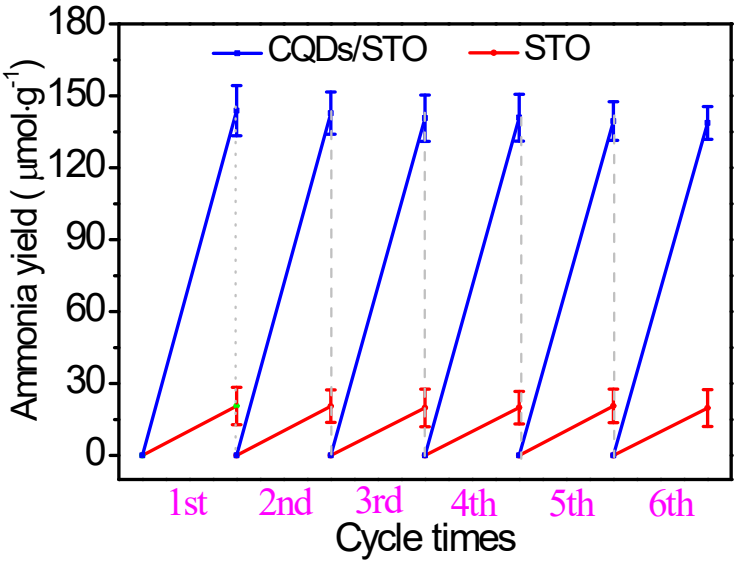

Figure S5. The time-dependence of ammonia yield obtained after illumination under one sun irradiation. The error bars in every concentration are the standard deviation of at least three replicates of independent measurements.

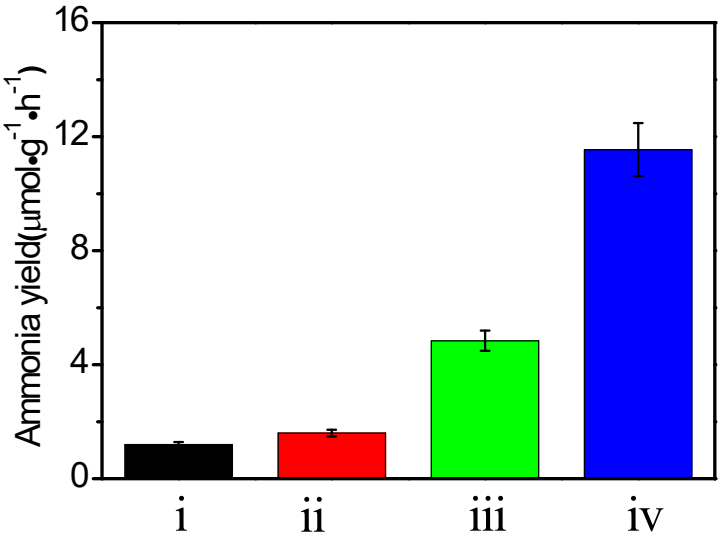

Figure S6. Yield rate of ammonia obtained on (i) STO and (ii) CQDs/STO (in Ar atmosphere under 1 sun illumination) and (iii) STO and (iv) CQDs/STO (in N_2 atmosphere in dark) over 12 h. The error bars in every concentration are the standard deviation of at least three replicates of independent measurements.

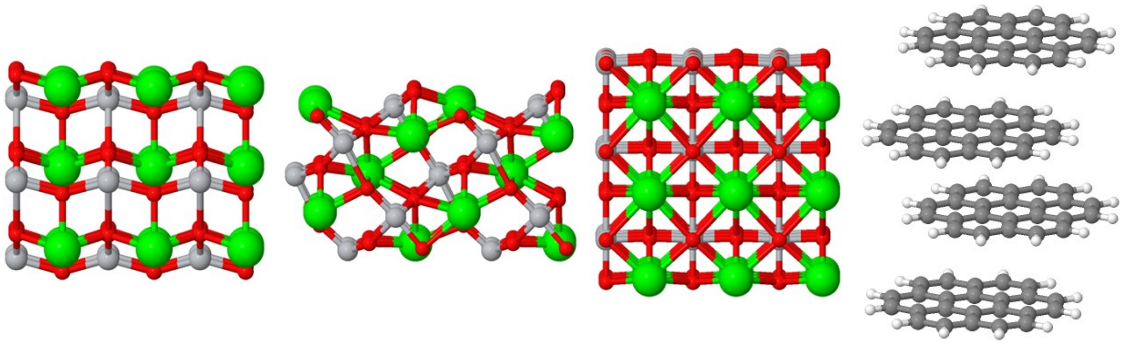

STO(110) STO(211) STO(200) CQD

Figure S7. Optimized structures of the models used for the DFT analysis. Defective STO and composite STO/CQD structures have been prepared from these ones.

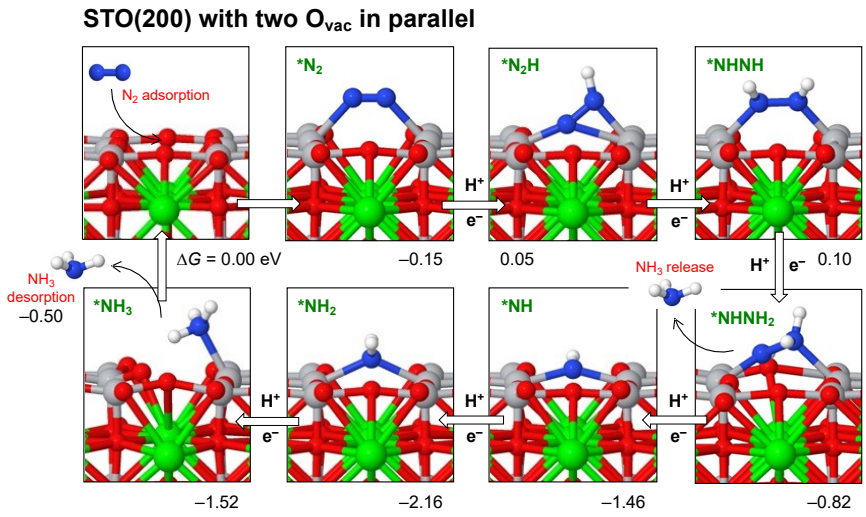

Figure S8. Proposed reaction mechanism for the electrochemical N_2 conversion into NH_3 catalyzed by the STO(200) surface with two O-vacancies in parallel. Note: reaction free energies at room temperature are shown in eV when there is no applied potential ($U = 0$) and pH = 0.

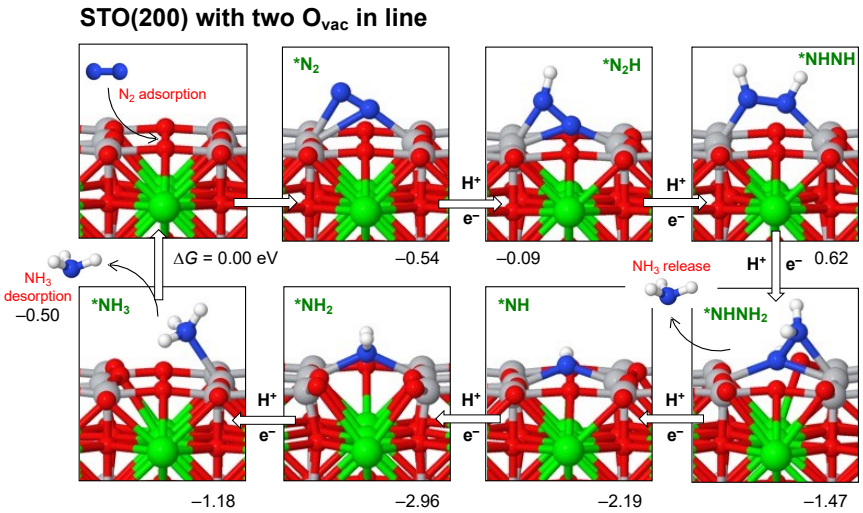

Figure S9. Proposed reaction mechanism for the electrochemical N_2 conversion into NH_3 catalyzed by the STO(200) surface with two O-vacancies in line. Note: reaction free energies at room temperature are shown in eV when there is no applied potential ($U = 0$) and pH = 0.

Computational details

The mechanism for the N_2 adsorption and its photo- and electrochemical conversion into NH_3 has been studied by means of density functional theory (DFT) through the generalized gradient approximation (GGA) with the Perdew-Burke-Ernzerhof (PBE) functional,[1] using a plane-wave cut-off energy of 400 eV.[2,3] The Brillouin zone (periodic boundary conditions) was sampled by 3×3×1 *k*-points using the Monkhorst-Pack scheme for STO and composite CQD/STO materials, while the Γ point was selected for the CQD. In order to avoid interactions between periodic slabs, a vacuum width of at least 10 Å was imposed. Optimization calculations were done using energy and force convergence limits equal to 10^{-4} eV/atom and |0.03| eV/Å, respectively. For gases, these energy and force cut-off criteria were set to 10^{-5} eV/atom and |0.001| eV/Å, respectively. Over these optimized geometries, band alignment calculations were performed using the Hyed-Scuseria-Ernzerhof functional[4] (HSE06, with 0.25 factor of exchange parameter) given the good harmony of this method between the hypothesized theoretical results with the experimental band gap and band energy positions for a variety of photocatalytic materials.[5] Finally, vibrational frequencies were calculated over Γ point in order to obtain zero-point energies (ZPE), thermal corrections, and entropy contributions. At this step, explicit dispersion correction terms to the energy were also employed through the use of the D3 method with the standard parameters programmed by Grimme and co-workers.[6,7] All optimization and vibrational frequency calculations have been performed throughout the facilities provided by the Vienna *Ab-Initio* Simulation Package (VASP, version 5.4.4).[8–11]

Modelling performance

Once the materials have been properly optimized, the NRR mechanism was investigated by optimizing the different states during N_2 conversion. Once N_2 is adsorbed on the catalytic surface ($*N_2$), a set of six H^+/e^- pair transfers occur; the first one leads to $*N_2H$, the second one to *NHNH or $*NNH_2$, and so on up to balance the chemical equation:

$$N_2(g) + 6\ H^+ + 6\ e^- \rightleftharpoons 2\ NH_3(g)$$

During optimization, no structural constrains have been applied. Over the optimized geometries, vibrational frequencies were calculated in order to obtain zero-point energies (ZPE), thermal corrections, and entropy contributions. In such cases, all metal atoms were frozen during vibrational frequency calculations, imposing no constrain on N and H atoms. At this stage, explicit D3 dispersion corrections were also applied.

In addition, free energy calculations have been carried out as follows:

$$G = E + \int C_P \, dT - TS$$

where G, E and C_P refer to the free energy, electronic energy, and heat capacity, respectively. The entropy term can be expressed as the sum of the translational, rotational, vibrational and electronic contributions as follows:

$$S = S_t + S_r + S_v + S_e$$

Finally, intrinsic zero-point energy (ZPE) and extrinsic dispersion (D) corrections were included to obtain this expression:

$$G = E + \int C_P \, dT - T(S_t + S_r + S_v + S_e) + \mathrm{ZPE} + D$$

Since $S_e \approx 0$ at the fundamental electronic level, Table S1 gathers the thermodynamic quantities for N_2, H_2 and NH_3 gases at standard conditions (298.15 K of temperature, 1 bar of fugacity for all gases).

Table S1. Thermodynamic quantities, in eV, for N_2, H_2 and NH_3 gases at standard condition (298.15 K, f = 1 bar) using PBE functional.

Gas	$E(+D)$	$\int C_P \, dT$	–TS	ZPE	G
$N_2(g)$	–16.70	0.09	–0.59	0.16	–17.04
$H_2(g)$	–6.75	0.09	–0.40	0.25	–6.81
$NH_3(g)$	–19.52	0.11	–0.59	1.03	–18.98

In the case of solids and adsorbates, some approximations can be assumed:

1. As for gases, at the fundamental electronic level $S_e \approx 0$.
2. Translational and rotational motions can be neglected, therefore, $S_t \approx 0$ and $S_r \approx 0$. In this sense, all entropy contributions come from vibrations: $S = S_v$. Similarly, translational and rotational contributions to the heat capacity are neglected.

Therefore, free energies for the different states along NRR have been calculated as to:

$$G = E + \int C_P \, dT - TS_v + ZPE + D$$

Finally, the reaction free energy between two states along the N_2 capture/conversion process carried out *via* electrochemical approach, *i*.e., $N_2(g) + 6\ H^+ + 6\ e^-(aq) \rightleftharpoons 2\ NH_3(g)$, can be expressed, by applying the proton-coupled electron transfer (PCET) approach,[12] as to:

$$\Delta G_R = G(*N_{2-m}H_{n-3m}) + mG(NH_3) - G(*) - G(N_2) - nG(H^+/e^-)$$

where '*' denotes the surface material, n is the number of H^+/e^- pairs transferred and m the number of NH_3 molecules released, if applicable (m = 0, 1). Obviously, for n = m = 0, the reaction free energy leads to the binding free energy:

$$\Delta G_b = G(*N_2) - G(*) - G(N_2)$$

In this regard, all energy values have been referred using the computational hydrogen electrode (CHE) model for the H^+/e^- transfer, considering the chemical potential of the H^+/e^- pair in aqueous solution as the half of the H_2 gas molecule at standard hydrogen electrode (SHE) conditions, *i.e.*, $f(H_2)$ = 1 bar, U = 0 V, and pH = 0, being $f(H_2)$ and U the fugacity of H_2 and the external potential applied, respectively.

$$\mu(H^+/e^-) = ½\ \mu\ (H_2)$$

And therefore, ΔG_R can be expressed as to:

$$\Delta G_R = G(*N_{2-m}H_{n-3m}) + mG(NH_3) - G(*) - G(N_2) - n/2\ G(H_2)$$

References

1 J. P. Perdew, K. Burke and M. Ernzerhof, *Phys. Rev. Lett.*, 1996, **77**, 3865–3868.

2 P. E. Blöchl, *Phys. Rev. B*, 1994, **50**, 17953–17979.

3 G. Kresse and D. Joubert, *Phys. Rev. B*, 1999, **59**, 1758–1775.

4 J. Heyd, G. E. Scuseria and M. Ernzerhof, *J. Chem. Phys.*, 2003, **118**, 8207–8215.

5 M. Harb and L. Cavallo, *ACS Omega*, 2018, **3**, 18117–18123.

6 S. Grimme, J. Antony, S. Ehrlich and H. Krieg, *J. Chem. Phys.*, 2010, **132**, 154104.

7 S. Grimme, S. Ehrlich and L. Goerigk, *J. Comput. Chem.*, 2011, **32**, 1456–1465.

8 G. Kresse and J. Hafner, *Phys. Rev. B*, 1993, **47**, 558–561.

9 G. Kresse and J. Hafner, *Phys. Rev. B*, 1994, **49**, 14251–14269.

10 G. Kresse and J. Furthmüller, *Phys. Rev. B*, 1996, **54**, 11169–11186.

11 G. Kresse and J. Furthmüller, *Comput. Mater. Sci.*, 1996, **6**, 15–50.

12 A. A. Peterson, F. Abild-Pedersen, F. Studt, J. Rossmeisl and J. K. Nørskov, *Energy Environ. Sci.*, 2010, **3**, 1311–1315.